Article

Morphological Transformation of $NiCoMoSeO_x$ from Nanosheets to Nanorods for Enhanced Oxygen Evolution

Jianbin Luo [1,†], Xiaofei Long [1,2,†], Biao Huang [1], Lei Huang [1,3], Jing Cao [1], Qingdian Yan [1], Mao Wu [1], and Ming Zhao [1,3,*]

[1] Department of Materials Science & Engineering, National University of Singapore, Singapore 117575, Singapore
[2] Key Laboratory of Low-Grade Energy Utilization Technologies and Systems, Ministry of Education of China, Chongqing University, Chongqing 400044, China
[3] Centre for Hydrogen Innovations, National University of Singapore, Singapore 117580, Singapore
* Correspondence: mingzhao@nus.edu.sg
† These authors contributed equally to this work.
Received: 10 August 2025; Revised: 29 September 2025; Accepted: 10 October 2025; Published: 13 October 2025

Abstract: Green hydrogen production via water electrolysis has emerged as a promising technology to address the environmental crisis and to achieve sustainability. However, the anodic oxygen evolution reaction (OER) of water electrolysis is kinetically sluggish, which requires the development of highly efficient catalysts to materialize this technology. Herein, we report the facile synthesis of two-dimensional $NiCoMoSeO_x$ nanosheets, which can be further transformed into one-dimensional nanorods. Structural characterizations confirm the existence of amorphous and crystalline domains in the nanosheets while the nanorods feature high crystallinity. The progressive nanosheets-to-nanorods transformation was also accompanied with composition variation and further oxidation. Excitingly, when employed as catalysts for alkaline OER, the nanorods exhibit a dramatic overpotential drop of 123 and 158 mV at 10 and 200 mA cm^{-2}, respectively, relative to the nanosheet counterpart. Moreover, the nanorods also exhibit superior durability than the nanosheets at various current density and could largely maintain its performance for 200 h at 300 mA cm^{-2}. In situ spectroscopic analysis confirms the critical role of low-valence Mo species in suppressing the Se leaching from nanorods, which greatly stabilizes the structure for improved durability. This work offers an effective approach to produce nanorods via structural transformation, together with valuable insights into the structure-performance relation for enhanced electrocatalysis.

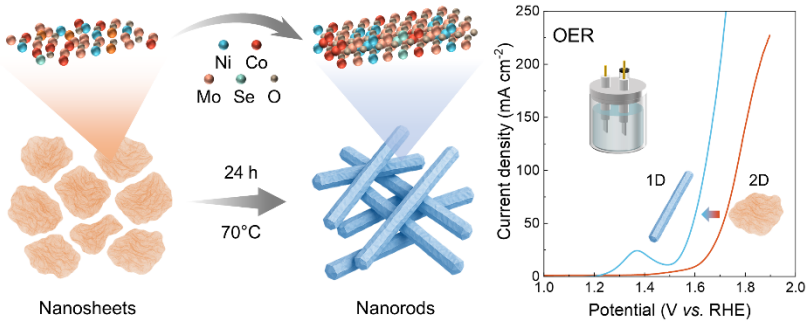

Keywords: oxygen evolution reaction; nanosheets; nanorods; structural transformation; structure-performance relationship

1. Introduction

Water electrolysis using green electricity has received considerable attention owing to the capability to produce green hydrogen and the potential to integrate with renewable energy devices for value-added chemicals synthesis [1–5]. However, the sluggish kinetics of the anodic oxygen evolution reaction (OER) of water electrolysis, which involves a complex four-electron pathway and thus impose a substantial activation energy barrier, largely retarding the practical application of this technology [6–8]. To this end, tremendous efforts have been devoted to the development of OER catalysts, with effective methods encompassing phase engineering [9–11], composition optimization [12–14], and morphological control [15–18].

Among various catalysts, noble metal-based catalysts, such as RuO_2 and IrO_2, have demonstrated exceptional OER performance. However, their extremely low abundance and notoriously high cost hinder their large-scale applications [13]. To address these limitations, extensive efforts have been invested in exploring earth-abundant

transition metal-based catalysts, such as Ni and Co. Notably, the catalytic activity of those catalysts is highly sensitive to the morphology [19–21], which defines the nature of catalytically active sites involved in reactant adsorption and electron transfer [22–24]. As a compelling example, Sun and co-worker reported a porous nanoscale $NiO/NiCo_2O_4$ heterostructure which optimize the mass transfer process and significantly increases the electrochemically active surface area (ECSA) compared to NiO particles, collectively contributing to the improved catalytic activity [25]. Despite the progress, the catalytic performance of the abundant metal-based catalysts is still unsatisfactory, which calls for the further improvement of highly efficient catalysts. One promising strategy for enhancing the efficiency of catalysts is to engineer the morphology and dimensionality of nanocatalysts. However, the current understanding of dimensionality-controlled nanomaterials remains insufficient, and their structure-performance relationships necessitate further investigation.

Herein, we successfully synthesized the two-dimensional (2D) $NiCoMoSeO_x$ nanosheets and subsequently, the one-dimensional (1D) $NiCoMoSeO_x$ nanorods via the dimensional transformation from 2D nanosheets. Specifically, Ni, Co, and Mo were employed owing to their outstanding activity toward OER [19–21], while Se nanoparticles serve as the reductant to induce the formation of multi-metallic oxides, which also plays a key role in the morphological transformation. The nanosheets were proven to consist of both amorphous and crystalline domains while the nanorods were highly crystallized. The transformation mechanism from nanosheets to nanorods was also investigated through the time-dependent monitoring of products and composition analysis. When used as catalysts toward OER in alkaline conditions, the 1D nanorods show greatly enhanced activity and durability than the 2D nanosheets. Additionally, in situ attenuated total reflection surface-enhanced infrared absorption spectroscopy (ATR-SEIRAS) was conducted to rationalize the enhanced catalytic performance and reaction mechanisms.

2. Methods and Characterizations

2.1. Chemicals and Materials

Ethanol (C_2H_5OH, 99%) was obtained from J.T. Baker. Sodium sulfite (Na_2SO_3, 98%) was obtained from Thermo Fisher Scientific. Pt/C (20 wt.%) was obtained from Johnson Matthey. Sodium tetrachloroaurate (III) ($NaAuCl_4$, 99.9%) was obtained from Macklin. Selenous acid (H_2SeO_3, 98%), hydrazine hydrate ($N_2H_4 \cdot H_2O$, 50–60% in H_2O) and potassium hydroxide (KOH, 99.99%) were obtained from Sigma Aldrich. Nickel chloride hexahydrate ($NiCl_2 \cdot 6H_2O$, 99.9%), sodium molybdate (Na_2MoO_4, 99%), cobalt chloride ($CoCl_2$, 99%), sodium thiosulfate pentahydrate ($Na_2S_2O_3 \cdot 5H_2O$, 99.99%), ammonium chloride (NH_4Cl), hydrofluoric acid (HF, 2% aqueous solution), polyvinylpyrrolidone (PVP, MW ≈ 55,000) were all obtained from Aladdin. Nafion® aqueous solution (N–117, 5wt.%, Dupont), nickel foam (Sinero) and carbon paper (Toray) were used as received. Millipore deionized (DI) water with resistivity of 18 MΩ cm was used for preparing all solutions unless specified.

2.2. Syntheses of $NiCoMoSeO_x$ Nanosheets and Nanorods

The synthesis of $NiCoMoSeO_x$ nanosheets include two major steps. In the first step, Se nanoparticles were prepared based on a reported protocol [26,27]. Typically, 0.3 mmol of H_2SeO_3 and 10 mg of PVP were mixed and dissolved in 10 mL of DI water under magnetic stirring for 10 min, followed by a one-shot injection of 414 μL of $N_2H_4 \cdot H_2O$ at room temperature. After 3 h, the as-synthesized Se nanoparticles were collected via centrifugation at 12,000 rpm for 20 min and washed three times with DI water and then dispersed in 10 mL of DI water for further use. In the second step, 0.6 mmol of $NiCl_2$, 0.2 mmol of $CoCl_2$, and 0.2 mmol of Na_2MoO_4 were dissolved in 10 mL DI water in a 20-mL glass vial and stirred for 10 min, followed by one-shot injection of 2 mL of the as-prepared Se nanoparticles suspension. The mixture was heated at 70 °C for 3 h in oil bath. The products were collected via centrifugation at 10,000 rpm for 5 min and then washed with DI water three times. The synthesis of $NiCoMoSeO_x$ nanorods follows the same protocol except extending the reaction to 24 h.

2.3. Characterizations

Scanning transmission electron microscope (STEM) and energy-dispersive X-ray spectroscopy (EDS) elemental mapping images were acquired on a JEOL JEM-F200 microscope. TEM images and selected area electron diffraction (SAED) patterns were acquired on a JEOL JEM-2010F microscope. X-ray photoelectron spectroscopy (XPS) spectra were measured using a Thermo scientific ESCALAB 250Xi XPS microprobe. All photochromic tests were conducted under ambient conditions.

2.4. Electrochemical Measurements

All the electrochemical measurements were conducted in a three-electrode cell using an electrochemical workstation (CS310X, Corrtest). A carbon rod and saturated calomel electrode (SCE) were used as the counter and reference electrode, respectively. Working electrodes were prepared by dropping various catalyst inks on the carbon paper. Specifically, catalyst inks were prepared as follows: 15 mg of as-synthesized $NiCoMoSeO_x$ was dispersed in the mixture of 2 mL ethanol and 1 mL DI water. The mixed solution was treated with ultrasonication for 5 min, followed by the addition of 60 μL 5wt.% Nafion solution. After an additional 1-h ultrasonication, 200 μL of prepared ink was dropped onto the carbon paper, forming a working electrode with active aera of 0.5 cm^2.

Linear sweep voltammograms (LSVs), cyclic voltammograms (CVs), electrochemical impedance spectroscopy (EIS), and chronopotentiometric tests were conducted in a 1 M KOH aqueous solution. For LSVs, the potential range was set at 1.0–1.9 V vs. RHE at a scan rate of 5 mV s^{-1}. The potentials were derived from *E*(SCE) and presented as *E*(RHE), according to the formula:

$$E(\mathrm{RHE}) = E(\mathrm{SCE}) + 0.2412 + 0.05916 * pH \quad (1)$$

CVs were conducted at scan rates of 10, 20, 40, 60, 100 mV s^{-1} within the non-Faradaic region (0.1–0.2 V) to calculate the double layer capacity (C_{dl}). The C_{dl} were calculated using the following formula:

$$C_{\mathrm{dl}} = \frac{\Delta i}{2\nu} \quad (2)$$

where $\Delta i/2$ represents the capacitive current at a specific potential, and ν is the CV scan rate.

To quantify the ECSA and specific activity (i_s), the specific capacitance (C_s) with typical value of 40 μF cm^{-2} for NiCo-based alloys, and the current density measured by LSV (i_{LSV}) are introduced in the following equation [28]:

$$\mathrm{ECSA} = \frac{C_{\mathrm{dl}}}{C_{\mathrm{s}}} \quad (3)$$

$$i_{\mathrm{s}} = \frac{i_{\mathrm{LSV}}}{\mathrm{ECSA}} \quad (4)$$

EIS was conducted in the three-electrode system at 1.75 V vs. RHE which falls in the active reaction region. Herein, both Nyquist and Bode plots were obtained with frequency range from 10,000 to 1 Hz and sinusoidal potential perturbation amplitude of 5 mV.

To accommodate long-term stability testing, the working electrode substrates were replaced with nickel foam, while all other experimental conditions remained unchanged. The as-synthesized catalysts were subjected to stepwise chronopotentiometric stability tests at 10, 20, and 50 mA cm^{-2}, with each step lasting 20 h. In addition, to evaluate the durability of the nanorods under high current density, an extended chronopotentiometric test was performed at 300 mA cm^{-2} for 200 h.

2.5. In Situ ATR-SEIRAS Study

All in situ ATR-SEIRAS spectra were recorded on a Fourier-transform infrared (FTIR) spectrometer (iS50, Thermo Fisher Scientific) equipped with a liquid-nitrogen-cooled MCT detector. Unless otherwise noted, measurements were conducted at an incident angle of 60°, with a spectral resolution of 8 cm^{-1} and averaged over 100 scans. The obtained spectra are presented in terms of reflectance, as defined by:

$$\frac{\Delta R}{R} = \frac{R(E_1) - R(E)}{R(E)} \quad (5)$$

where $R(E_1)$ and $R(E)$represent the reflectivity from the electrode at the applied potential E_1 and open circuit potential, respectively.

The homemade reaction cell was set as the Kretschmann configuration, with the catalyst drop-casting onto the Si prism coated with an Au film. The protocol for coating an approximately 50 nm Au film on Si prism follows previous report [29]. Residual material on the prism surface was removed by aqua regia, after which the prism was rinsed with deionized water and polished using 0.05 μm abrasive powder. A 40% NH_4F solution was then applied to the surface for several minutes to remove the native oxide layer [30]. Au deposition was performed at 60 °C by drop-casting a plating solution (0.015 M $NaAuCl_4 \cdot 2H_2O$, 0.15 M Na_2SO_3, 0.05 M $Na_2S_2O_3 \cdot 5H_2O$, and 0.05 M NH_4Cl) mixed with 2% HF in a 2:1 volume ratio onto the Si surface. Using the CHI 660e electrochemical workstation, the potentials ranged from 1.0 to 1.9 V vs. RHE were applied to induce OER while the spectra were recorded from 4000 to 650 cm^{-1}. Each infrared spectrum was collected after holding the potential constant for 5 min.

3. Results and Discussion

3.1. Synthesis and Characterizations of $NiCoMoSeO_x$ Nanosheets

The one-pot synthesis of $NiCoMoSeO_x$ nanosheets was accomplished by the galvanic replacement reaction between Se nanoparticles and Ni(II), Co(II), and Mo(VI) precursors. First, Se nanoparticles were synthesized as the template, with an average diameter of 37.5 ± 1.4 nm (Figure S1) [26,27]. After the galvanic replacement reaction at 70 °C for 3 h, nanosheets with abundant wrinkles and basal planes were obtained, as evidenced by the TEM images (Figure 1a,b). The lattice fringe spacings of 2.21 and 2.59 Å can be indexed to the (200) and (111) plane, close to 2.10 Å of the (200) plane and 2.41 Å of the (111) plane in $Ni_{0.5}Co_{0.5}$ oxide [31], suggesting the formation of multi-metallic oxides ($NiCoMoSeO_x$, Figure 1c). The wrinkles within the nanosheets presented an average size of 2.9 ± 0.8 nm in width (Figure 1d). Regarding the basal plane, high-resolution STEM image showed a mix of amorphous and crystalline domains (Figures 1e and S2). Within the crystalline domains, the lattice fringe spacings of 2.17 and 2.56 Å correspond to the (111) and (110) planes of $NiCoMoSeO_x$, similar to those of the wrinkles and suggesting identical compositions (Figure 1e). In addition, the presence of crystalline structure was also confirmed by the SAED rings indexed to (110), (111), and (200) reflections of the crystalline constituents of $NiCoMoSeO_x$ (Figure 1f), consistent with the results shown in Figure 1e. To analyze the composition of the nanosheets, we conducted EDS elemental mapping. As shown in Figure 1g, the atomic proportions of Ni, Co, Mo, Se, and O are 12.46%, 11.51%, 16.50%, 0.03%, and 59.50%, respectively, revealing the oxide structure of the nanosheets. Moreover, the extremely low composition of Se in the nanosheets validates the role of Se nanoparticles as a sacrificial template for the galvanic replacement, where Se atoms were oxidized and dissolved in the solution as cations (Figure S3). It is worth noting that the Se nanoparticles cannot be completely oxidized without the Mo^{6+} precursor (Figure S4). The galvanic replacement reaction can be further supported by the thermodynamic potential of Se^0/Se^{4+} (−0.74 V vs. standard hydrogen electrode or SHE), which is lower than those of Mo^{6+}/MoO_2 (+0.02 V), Ni^{2+}/Ni (−0.257 V), and Co^{2+}/Co (−0.277 V). Moreover, UV-Vis spectroscopic analysis suggest that the absorption peak intensity of Se nanoparticles at 283 nm shows a clear decay over the reaction time upon the addition of the Ni^{2+} precursor (Figure S3), further confirming the occurrence of galvanic replacement. Figures 1h and S5 shows the EDS mapping of Ni, Co, Mo, Se, and O distributions, indicating uniform distributions across the nanosheet.

3.2. Synthesis of Characterizations of $NiCoMoSeO_x$ Nanorods

Excitingly, when the standard synthesis was extended from 3 to 24 h, the obtained products were switched from nanosheets to nanorods, as shown in Figure 2a. Specifically, the nanorods are uniform and in high quality, with an average size of 36.4 ± 14.8 nm (Figures 2a–d, and S6). Different from the mixed amorphous/crystalline structure in the nanosheets, the as-obtained nanorods possess a well crystalline structure (Figure 2b–e). Specifically, the lattice fringes in the nanorods are derived as 1.75, 1.83, and 2.98 Å, corresponding to the (200), (111), and (110) planes of $NiCoMoSeO_x$ (Figure 2e). The structural ordering was further corroborated by the SAED pattern, which displays sharp, discrete diffraction rings indexed to the (100), (110), (111), and (200) planes that are indicative of a highly crystalline lattice (Figure 2f). It is worth noting that compared to nanosheets, the nanorods show slightly reduced (200) and (111) lattice fringe spacings, which we attribute to the higher crystallinity and thus more compact atom packing in nanorods [32]. XRD patterns of nanosheets and nanorods indicate the low and high crystallinity (Figure S8), respectively, with the characteristic peaks close to those of NiO, MoO_3, Co_3O_4 and SeO_2. Moreover, the composition difference could also contribute to the variation of lattice fringe spacings. As shown in Figure 2g, the atomic proportions of Ni, Co, Mo, Se, and O are 6.06%, 9.03%, 15.95%, 0.16%, and 68.80%, respectively, showing a higher O proportion than that of nanosheets. The increased O portion in the nanorods suggests the continuous oxidation of the nanosheets over the extended reaction time. EDS mapping results show the uniform distributions of Ni, Co, Mo, Se, and O in the nanorods, confirming the homogeneous composition across the nanorods (Figures 2h and S8).

3.3. Dynamic Structural Evolution from Nanosheets to Nanorods

To elucidate the transformation mechanism from nanosheets to nanorods, we collected the products synthesized via the standard protocol except for reaction at 3, 6, 12, 18, and 24 h, as summarized in Figure 3a–e. After 3 h of reaction, i.e., the standard synthesis, the as-obtained products were predominant by nanosheets. Upon extending the reaction to 6 h, nanorods started to appear, showing a proportion of 44% (Figure 3b). Other than the nanorods with large sizes, we also observed some small nanorods mixed with nanosheets, suggesting the ongoing transformation from nanosheets to nanorods (Figure 3b). Especially, these intermediate small nanorods show similar structure and size to those of the wrinkles in the nanosheets (Figures 1b,c and 3a,b), suggesting that the

structural transformation might start from the wrinkles. When the reaction was extended for 12 and further to 18 h, the proportion of nanorods in the product increased remarkably to 84% and 86%, respectively (Figure 3c,d,f). Eventually, highly pure and uniform nanorods with almost 100% were obtained after 24 h of reaction (Figure 3e,f).

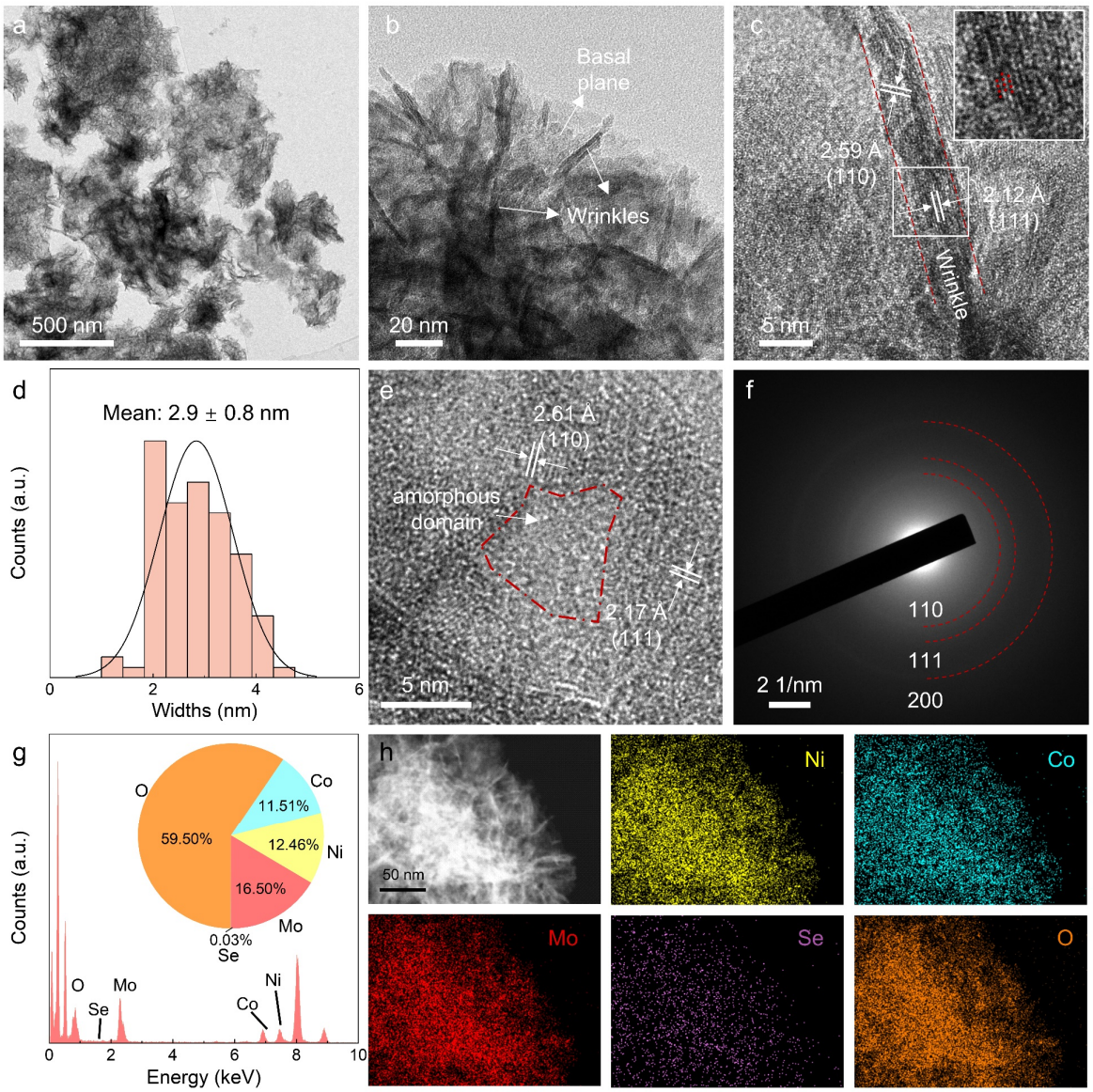

Figure 1. Synthesis and characterizations of $NiCoMoSeO_x$ nanosheets. (**a–c**) STEM images of $NiCoMoSeO_x$ nanosheets at different magnifications. The two parallel red dashed lines define the width of wrinkles. (**d**) The width distribution of wrinkles, which is 2.9 ± 0.8 nm. (**e**) High-resolution STEM and (**f**) SAED pattern of $NiCoMoSeO_x$ nanosheets displaying mixed domains with different lattice phases. (**g**) EDS survey of Ni, Co, Mo, Se, and O. (**h**) EDS elemental mapping of Ni, Co, Mo, Se, and O distributions in the $NiCoMoSeO_x$ nanosheets. The scale bar applies to all panels in (**h**).

To investigate the electronic structures of $NiCoMoSeO_x$ nanosheets and nanorods, we conducted XPS analysis. The survey spectra reveal the presence of Ni 2*p*, Co 2*p*, Mo 3*d*, Se 3*d* and O 1*s* in both nanosheets and nanorods (Figure 4a). In the high-resolution Ni 2*p* spectrum of nanosheets, two characteristic peaks at 873.4 and 875.1 eV are observed, corresponding to Ni^{2+} $2p_{1/2}$ and Ni^{3+} $2p_{1/2}$, respectively (Figure 4b) [33]. Notably, the Ni^{3+} $2p_{1/2}$ peak shifts by +0.8 eV from nanosheets to nanorods, which we attribute to that Ni was coordinated by a greater proportion of oxygen atoms (Figure 4b). Similarly, Co 2*p* spectrum reveals presences of Co^{2+} and Co^{3+} at 780.6 and 782.9 eV, respectively (Figure 4c). In comparison, the major peaks at 235.5 and 232.3 eV are assigned to the Mo^{4+} $3d_{3/2}$ and $3d_{5/2}$, respectively, rather than Mo^{6+}. This suggests that Mo^{6+} in the precursors was predominately reduced to Mo^{4+} during the formation of $NiCoMoSeO_x$ nanosheets and nanorods (Figure 4d). Moreover, both Mo^{4+} $3d_{3/2}$ and $3d_{5/2}$ peaks negatively shift by 0.1 eV after transforming into nanorods, the electron transfer from Mo to the neighboring atoms (Figure 4d). We also found that there exists Se^0 in the nanosheets, as

evidenced by the characteristic peaks at 56.4 eV and 55.8 eV, suggesting that the residual of Se^0 in the nanosheets (Figure 4e). Surprisingly, only characteristic peaks of SeO_x were observed in the nanorods after morphological transformation (Figure 4e). This sharp contrast indicates that the residual Se^0 atoms were further oxidized during transformation of nanosheets into nanorods. Additionally, the metal oxide lattice oxygen (O_m) peak shows a negative shift of 0.5 eV after nanosheets-to-nanorods transformation while the surface –OH/–OOH peak (O_{OH}) suggest a positive shift of 0.5 eV. This observation likely results from the strengthened interaction between high-valence metal centers and hydroxyl species in the more crystallized nanorods (Figure 4f).

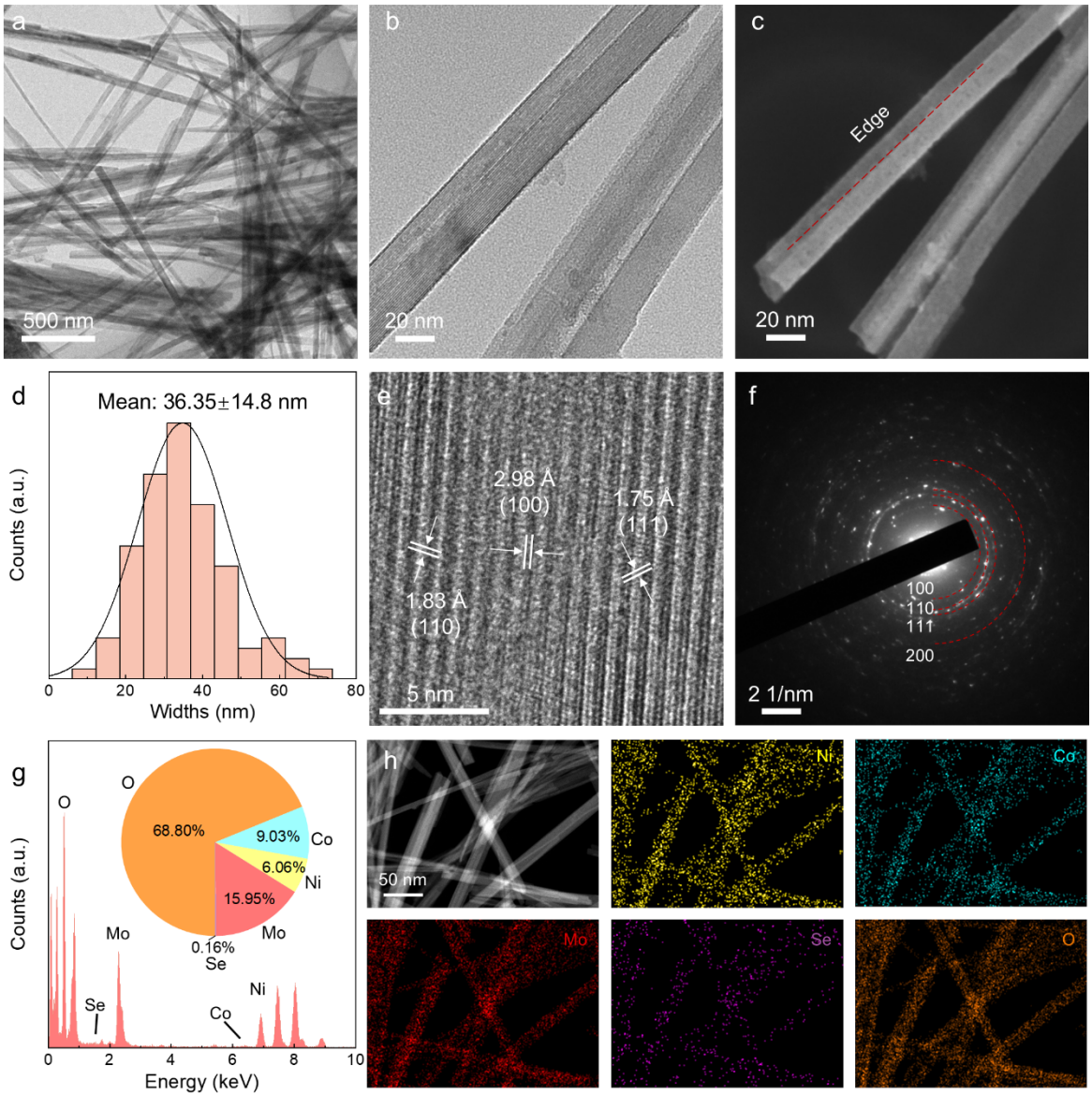

Figure 2. Synthesis and characterizations of $NiCoMoSeO_x$ nanorods. (**a–c**) STEM images of $NiCoMoSeO_x$ nanorods at different magnifications. (**d**) Size distribution of nanorods, which is derived as 36.4 ± 14.8 nm. (**e**) High-resolution STEM and (**f**) SAED pattern of a representative local plane structure in $NiCoMoSeO_x$ nanorods. (**g**) EDS survey of Ni, Co, Mo, Se, and O elements. (**h**) EDS elemental mapping of Ni, Co, Mo, Se, and O distributions in the $NiCoMoSeO_x$ nanorods. The scale bar applies to all panels in (**h**).

3.4. Enhanced Performance and Stability After the Transformation

The synthesis of $NiCoMoSeO_x$ nanosheets and nanorods allows us to study the structure-dependent catalytic properties toward alkaline OER in 1 M KOH electrolyte. As shown in the LSV curves, the nanorods demonstrate markedly enhanced OER activity compared to the nanosheets, requiring lower overpotentials to reach the same current density (Figure 5a). Specifically, the overpotential at 10 mA cm^{-2} was reduced from 383 to 260 mV after the nanosheets-to-nanorods transformation, showing a dramatic drop of 123 mV. This notable overpotential drop was maintained and even enlarged at high current density of 50, 100, and 200 mA cm^{-2}, with the overpotential drop of

119, 126, and 158 mV, respectively, further confirming the superior OER performance of the nanorods (Figure 5b). Moreover, the Tafel slope analysis suggests that the nanorods exhibit a Tafel slope of 119.45 mV dec^{-1}, which is lower than 147.06 mV dec^{-1} for the nanosheets, indicating faster reaction kinetics during OER (Figure 5c). Notably, a distinct current peak appears in the potential range of 1.2–1.5 V vs. RHE for nanorods, whereas no such response is observed for nanosheets (Figure 5a). This difference likely stems from the lower initial oxidation states of Mo in nanorods than in nanosheets, making it vulnerable to be further oxidized under high positive potentials (Figure 4d).

To uncover the origin of enhanced OER activity, we analyzed the ECSAs of nanorods and nanosheets by measuring the C_{dl} (Figure S9a,b). The calculated results show that the C_{dl} of nanosheets and nanorods is 2.1 and 4.6 mF cm^{-2}, respectively, suggesting that more active sites are exposed on the nanorods than on the nanosheets, thus leading to the enhanced OER activity (Figure 5d). Figure S7c shows the C_{dl}-normalized LSV curves, where the nanorods still exhibit higher specific activity than nanosheets, implying that the performance enhancement could not be exclusively attributed to the larger ECSA. We then conducted EIS to investigate the conductivity and the charge transfer kinetics of both $NiCoMoSeO_x$ nanosheets and nanorods, with the resulting Nyquist plots fitted using the equivalent circuit (Figure 5e) [34]. Specifically, the charge transfer resistance R_{ct} of nanorods is 7.15 Ω cm^2, much lower than 13.26 Ω cm^2 for the nanosheets. This lower charge transfer resistance could promote electron transfer during OER, resulting in faster reaction kinetics and thus higher current density. To further understand the role of R_{ct} in affecting the OER activity, we conducted EIS measurements under operando OER conditions in a potential range of 1.65 to 1.9 V, where the OER kinetics are notable (Figures 5a and S10). Especially, the nanorods exhibited a R_{ct} value of 18 Ω cm^2 at 1.65 V, which is ~5.8 times lower than that of the nanosheets (105 Ω cm^2). In addition, the Bode-phase diagram shows that the nanorods exhibit a phase angle peak at a higher frequency (286 Hz) compared to the nanosheets (112 Hz, Figure 5f). Since in an equivalent circuit the characteristic frequency inversely correlates to R_{ct}, the higher peak frequency enabled by the nanorods suggests accelerated charge-transfer dynamics. which is attributed to the highly crystalline lattice and the 1D structure and continuous electron pathways with minimal boundary/defects scattering (Figure 5e) [35,36]. In contrast, the nanosheets exhibit a mixed crystalline/amorphous microstructure that disrupts long-range electron conduction, leading to increased charge transfer resistance [37].

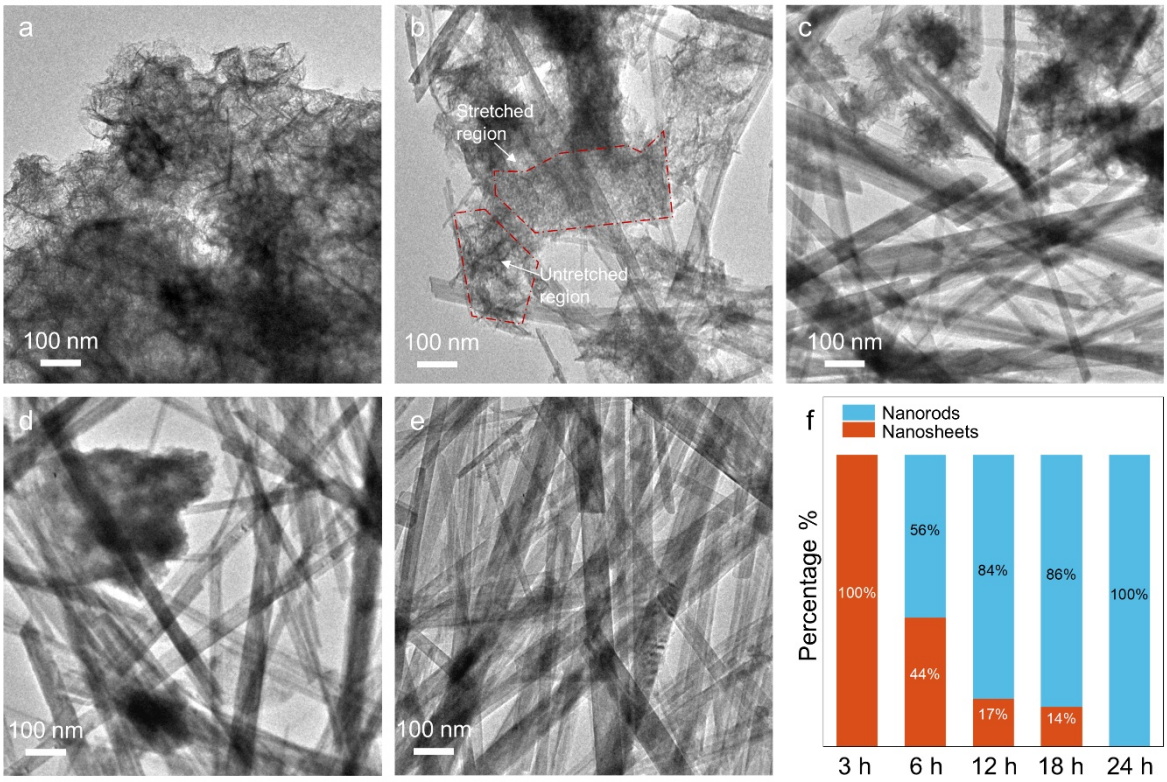

Figure 3. Time-dependent morphological evolution of $NiCoMoSeO_x$. (**a**–**e**) TEM images of the products obtained using the standard protocol but after reaction for (**a**) 3 h, (**b**) 6 h, (**c**) 12 h, (**d**) 18 h, and (**e**) 24 h. (**f**) Time-dependent distributions of nanosheets and nanorod in the products. The percentage of nanorods and nanosheets was estimated based on their projected areas in the TEM images.

To assess long-term durability, chronopotentiometric testing was conducted at 10, 20, and 50 mA cm^{-2} for 20 h (Figure 5g). Under all current densities, the nanorods show lower potentials than the nanosheets, validating the superior OER activity. Moreover, the nanorods exhibited decay rates of 3.1, 3.8, and 5.1 mV h^{-1} at 10, 20, and 50 mA cm^{-2}, respectively, lower than 4.0, 4.7 and 6.3 mV h^{-1} for nanosheets, validating the enhanced stability of nanorods. Notably, the nanosheets display notable voltage fluctuations during the potential switching, which we attributed to structural instability of the amorphous domains that are more susceptible to reconstruct under high potentials. To further assess the stability of nanorods, we conducted a durability test at 300 mA cm^{-2} for 200 h (Figures 5h and S11). The nanorods could well maintain both its rod structure and activity over the long-term test (Figure S11), showing a decay rate of only 1.468 mV h^{-1}, demonstrating its great promise for practical applications [38–42].

3.5. Investigation for the Enhancement Attributed to the Transformation via In Situ ATR-SEIRAS

To investigate the reaction mechanisms, in situ ATR-SEIRAS analysis was conducted for nanosheets and nanorods in the potential range of 1.0–1.9 V vs. RHE. As shown in Figure 6a,b, the nanosheets exhibit no discernible O–H stretching signals at potentials below 1.4 V, whereas the nanorods display a distinct peak at ~3384 cm^{-1} corresponding to the adsorption of free OH groups. This contrast indicates that nanorods possess stronger OH adsorption than nanosheets and thus results in the presence of more available OH groups for enhanced OER kinetics. When the applied potential was gradually increased to 1.8 V, both the nanosheets and nanorods display a pronounced hydrogen-bonded water adsorption band, with the nanorods exhibiting a much higher intensity. Moreover, the band of nanorods undergoes a progressive redshift from 3284 to 3248 cm^{-1}, indicative of hydrogen-bond network disruption and reorganization under OER conditions. As comparison, the commercial Pt/C and RuO_2 exhibits only the free-water peak during OER, suggesting the weak interaction among the absorbed *OH species without hydrogen bond (Figures S12 and S13). Concurrently, the δ(H–O–H) peaks at 1626 cm^{-1} for $NiCoMoSeO_x$ nanorods is significantly stronger than that of nanosheets, confirming a stronger interaction of the nanorod catalyst with water and other *OH species and thereby facilitate the initialization of oxygen evolution (Figure 6a,b).

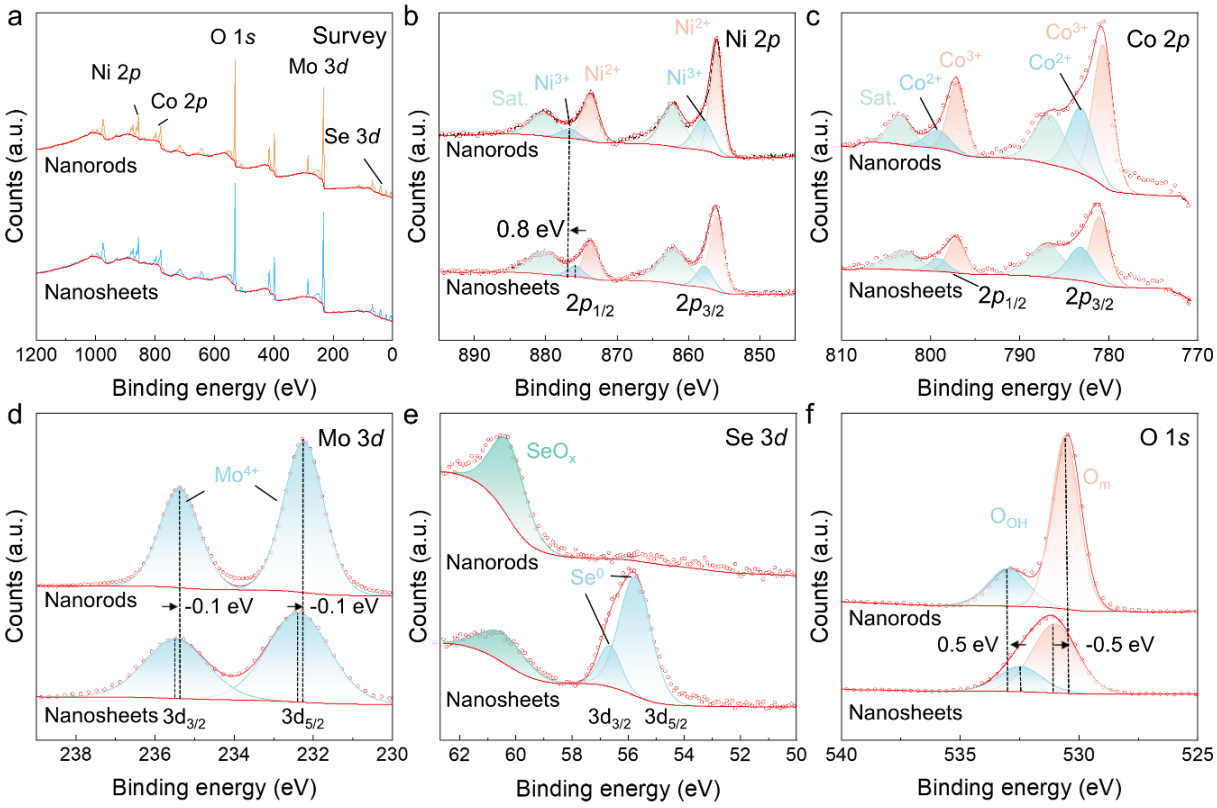

Figure 4. XPS of $NiCoMoO_x$ in nanosheets and nanorods morphologies. (**a**) Survey scan showing Ni, Co, Mo, Se and O signals. (**b**) Ni 2*p*, (**c**) Co 2*p*, (**d**) Mo 3*d*, (**e**) Se 3*d* and (**f**) O 1*s*. Black dashed vertical lines mark binding energy shifts in the nanosheets relative to nanorods.

In addition, M–O stretching vibrations were also observed in the low wavenumber region (Figure 6a–d). Both nanosheets and nanorods exhibited increasingly strong negative bands at 1242 cm^{-1} corresponding to Se–O vibrations with increasing potential. This indicated that Se–O species were partially leached from the lattice into the electrolyte

during OER, forming SeO_3^{2-} species that adsorbed onto the catalyst surface (Figure 6a–d). Importantly, due to the lower initial oxidation status of Mo content in the nanorods, distinct MoO_3^{2-} features appeared at 888 cm^{-1} during OER (Figure 6d). The greater proportion of relatively lower-valence Mo species in nanorods appeared to suppress Se leaching, helping to stabilize the structure and thereby improve the electrochemical durability. Moreover, the Raman spectroscopic analysis also indicates a characteristic Se–O peak at 283 cm^{-1} for the the $NiCoMoSeO_x$ nanorods after the durability test (Figure S14), with an intensity comparable to that of the pristine $NiCoMoSeO_x$ nanorods, confirming the suppressed leaching under long-term electrochemical tests.

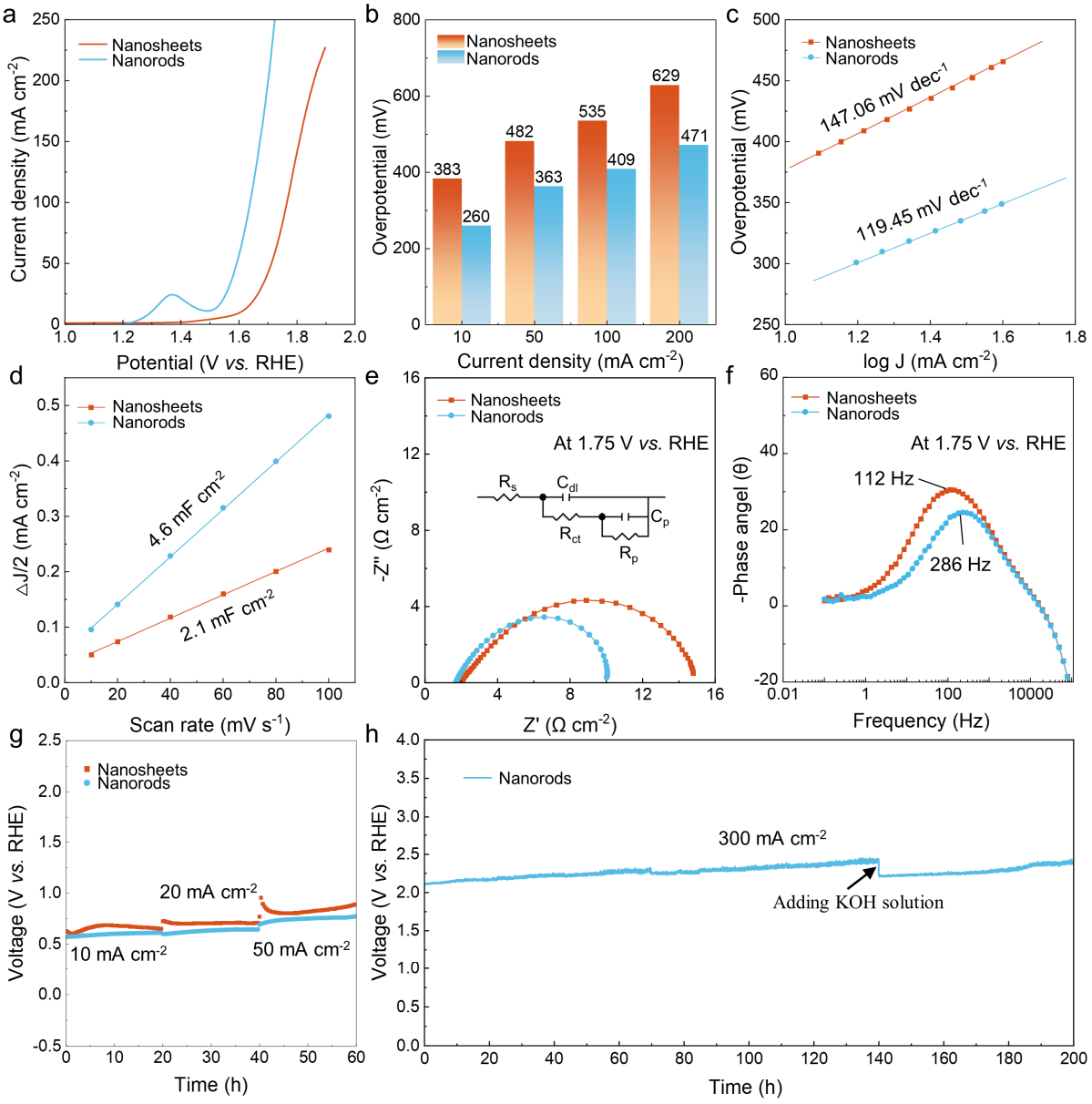

Figure 5. Electrochemical performance of nanosheets and nanorods in 1 M KOH. (**a**) LSV polarization curves (scan rate 5 mV s^{-1}, iR–corrected). (**b**) Overpotentials required to reach 10, 50, 100 and 200 mA cm^{-2}. (**c**) Tafel plots derived from (**a**). (**d**) Δj/2 vs. scan rate for C_{dl} determination. (**e**) Nyquist plots from EIS at 1.75 V vs. RHE and its equivalent circuit. (**f**) Bode-phase diagram from EIS at 1.75 V vs. RHE. (**g**) Chronopotentiometric stability at 10, 20 and 50 mA cm^{-2} over 60 h. (**h**) 200 h of durability test at 300 mA cm^{-2}, with KOH replenishment at 140 (**h**).

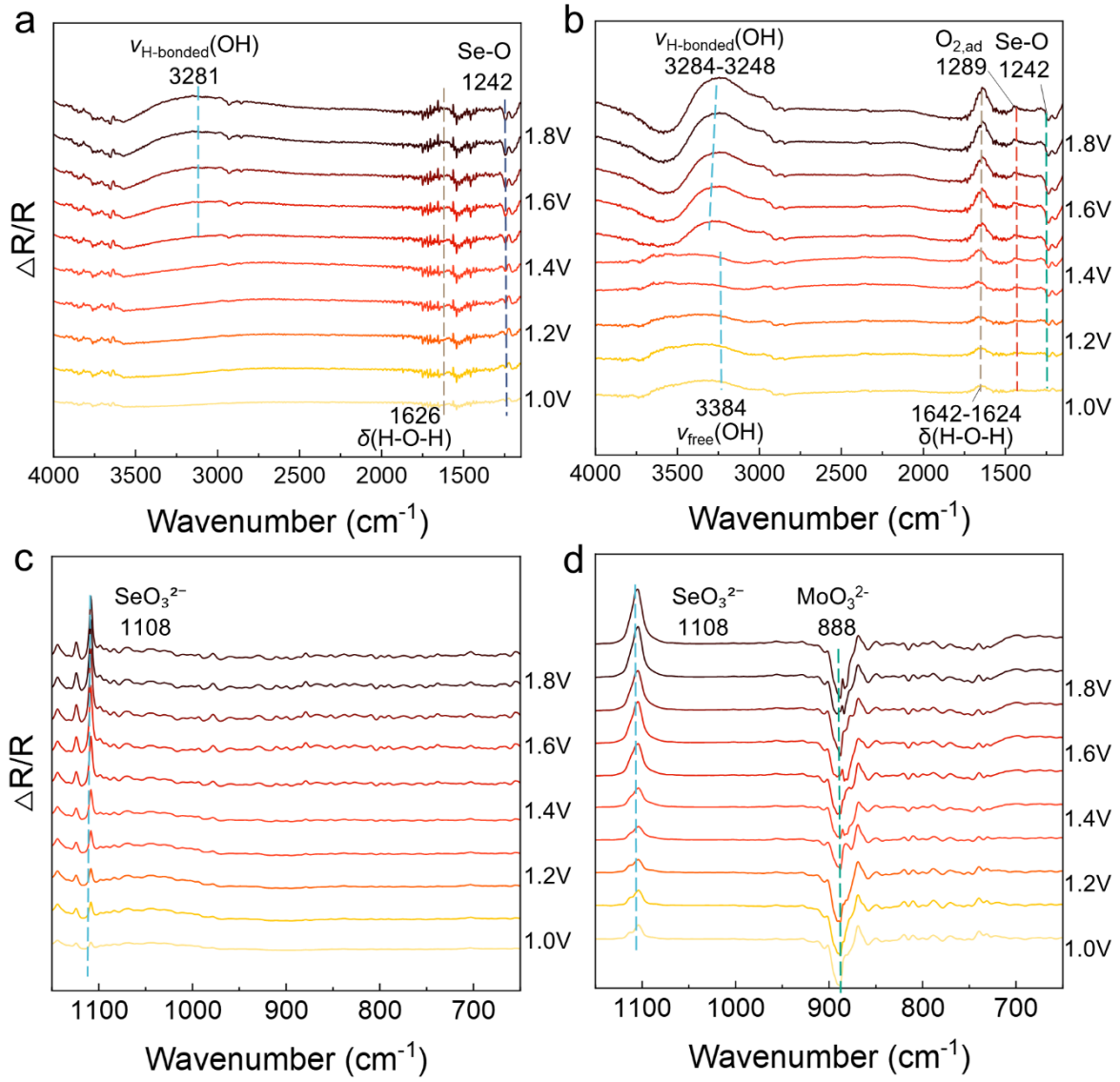

Figure 6. In situ ATR-SEIRAS ΔR/R spectra recorded at 1.0–1.9 V vs. RHE for $NiCoMoSeO_x$ nanosheets and nanorods: (**a**,**c**) nanosheets; (**b**,**d**) nanorods. (**a**,**b**) Full spectra in the range of 4000–1150 cm^{-1}. (**c**,**d**) Spectra of the fingerprint region (1150–650 cm^{-1}). Spectra are vertically offset for clarity.

4. Conclusions

In summary, we have demonstrated the successful synthesis of 2D $NiCoMoSeO_x$ nanosheets via galvanic replacement and their morphological transformation into 1D nanorods, simply by extending the reaction time. Accompanied with the dimensional transformation, the structure of the nanoparticles also evolved from mixed amorphous/crystalline structure in nanosheets to a highly crystallized structure in nanorods. Time-dependent analysis of the synthesis suggests that the structural transformation likely starts from the wrinkles of nanosheets, accompanied with the variations of composition and valence states of metal atoms. Significantly, this dimensional transformation resulted in a significant reduction of the overpotential from 383 to 260 mV at 10 mA cm^{-2}, when employed as catalysts for OER under alkaline conditions. EIS further revealed a pronounced decrease in charge transfer resistance from 13.26 for nanosheets to 7.15 Ω·cm^2 for nanorods, confirming the accelerated electron transfer kinetics in the 1D nanorod structure for enhanced catalysis. Long-term stability tests validated the excellent durability of $NiCoMoSeO_x$ nanorods, exhibiting insignificant performance degradation after 200 h of continuous operation at a high current density of 300 mA cm^{-2}. In situ ATR-SEIRAS study validates that the suppressed Se leaching by low-valence Mo species and thus a stabilized structure, lead to the superior electrochemical stability. We believe this work offers a new approach to regulate the dimension of nanocatalysts for enhanced OER and provides necessary insights into the structure-performance relationships, which collective contributes to the rational design of highly efficient electrocatalysts for sustainability applications.

Supplementary Materials: The following supporting information can be downloaded at: https://media.sciltp.com/articles/others/2510131446053079/MI-2508000264-Supplementary-Materials.pdf, Figure S1. TEM images of Se nanoparticles in low magnification (a) and high magnification (b) synthesized following reported studies [26,27]. The size of Se nanoparticles is 37.5 ± 1.4 nm. Figure S2. TEM images of $NiCoMoSeO_x$ nanosheets at low magnification (a) and high magnification (b). Figure S3. STEM image (a) and EDS elemental mapping of (b) Ni, (c) Co, (d) Mo, (e) Se, and (f) O distributions in the $NiCoMoSeO_x$ nanosheets. The scale bar applies to all panels in a. Figure S4. STEM images of $NiCoMoSeO_x$ nanorods at low magnification (a) and high magnification (b). Figure S5. HADDF-STEM image (a) and EDS elemental mapping of (b) Ni, (c) Co, (d) Mo, (e) Se, and (f) O distributions in the $NiCoMoSeO_x$ nanorods. The scale bar applies to all panels in a. Figure S6. CVs of (a) nanorods and (b) nanosheets in the non-active potential range with scan rates of 10, 20, 40, 60, 80, 100 mV s^{-1}. (c) Specific activity of nanosheets and nanorods normalized by C_{dl}. Figure S7. The Nyquist plots of nanosheets (a) and nanorods (b) measured at the range of 1.65–1.9 V. (c) The changes of R_{ct} upon different potentials derived from panel a and b. Figure S8. In situ ATR-SEIRAS spectra of RuO_2 during the OER at various potentials (1.0 V to 1.9 V). The spectra highlight key vibrational bands: the free OH stretching at 3384 cm^{-1}, H-O-H bending at 1643 cm^{-1}, and adsorbed *OOH at 1213 cm^{-1}. Figure S9. In situ ATR-SEIRAS spectra of Pt during the OER at various potentials (1.0–1.9 V). The spectra highlight key vibrational bands: the free OH stretching at 3384 cm^{-1}, H-O-H bending at 1642 cm^{-1}, and adsorbed O_2 at 1289 cm^{-1}. References [43,44] are cited in the Supplementary Materials.

Author Contributions: J.L. and X.L. conducted the nanoparticle synthesis and characterizations, electrochemical measurements, and data analysis. J.L. performed the in situ ATR-SEIRAS measurements. J.L. and M.Z. wrote the manuscript. M.Z. directed research. All authors contributed to discussions. All authors have read and agreed to the published version of the manuscript.

Funding: This work was supported by the National University of Singapore start–up grant, National Research Foundation, Prime Minister's Office, Singapore under its Campus for Research Excellence and Technological Enterprise (CREATE) programme (Development of advanced catalysts for electrochemical carbon abatement, project Code: 370184872), and Ministry of Education (grant no. 24-1770-A0002).

Data Availability Statement: The data that support the findings of this study are available from the corresponding author upon reasonable request.

Conflicts of Interest: The authors declare no conflict of interest.

References

1. Qian, Q.; Zhu, Y.; Ahmad, N.; Feng, Y.; Zhang, H.; Cheng, M.; Liu, H.; Xiao, C.; Zhang, G.; Xie, Y. Recent Advancements in Electrochemical Hydrogen Production via Hybrid Water Splitting. *Adv. Mater.* **2024**, *36*, 2306108. https://doi.org/10.1002/adma.202306108.
2. Sharshir, S.; Joseph, A.; Elsayad, M.; Tareemi, A.; Kandeal, A.; Elkadeem, M. A Review of Recent Advances in Alkaline Electrolyzer for Green Hydrogen Production: Performance Improvement and Applications. *Int. J. Hydrogen Energy* **2024**, *49*, 458–488. https://doi.org/10.1016/j.ijhydene.2023.08.107.
3. Tüysüz, H. Alkaline Water Electrolysis for Green Hydrogen Production. *Acc. Chem. Res.* **2024**, *57*, 558–567. https://doi.org/10.1021/acs.accounts.3c00709.
4. Sebbahi, S.; Assila, A.; Belghiti, A.; Laasri, S.; Kaya, S.; Hlil, E.; Rachidi, S.; Hajjaji, A. A Comprehensive Review of Recent Advances in Alkaline Water Electrolysis for Hydrogen Production. *Int. J. Hydrogen Energy* **2024**, *82*, 583–599. https://doi.org/10.1016/j.ijhydene.2024.07.428.
5. He, X.; Deng, B.; Lang, J.; Zheng, Z.; Zhang, Z.; Chang, H.; Wu, Y.; Yang, C.; Zhao, W.; Lei, M.; et al. Interfacial-Free-Water-Enhanced Mass Transfer to Boost Current Density of Hydrogen Evolution. *Nano Lett.* **2025**, *25*, 6780–6787. https://doi.org/10.1021/acs.nanolett.5c01235.
6. Lin, Y.; Dong, Y.; Wang, X.; Chen, L. Electrocatalysts for the Oxygen Evolution Reaction in Acidic Media. *Adv. Mater.* **2023**, *35*, 2210565. https://doi.org/10.1002/adma.202210565.
7. Li, H.; Lin, Y.; Duan, J.; Wen, Q.; Liu, Y.; Zhai, T. Stability of Electrocatalytic OER: From Principle to Application. *Chem. Soc. Rev.* **2024**, *53*, 10709–10740. https://doi.org/10.1039/d3cs00010a.
8. Chen, M.; Kitiphatpiboon, N.; Feng, C.; Abudula, A.; Ma, Y.; Guan, G. Recent Progress in Transition-Metal-Oxide-Based Electrocatalysts for the Oxygen Evolution Reaction in Natural Seawater Splitting: A Critical Review. *eScience* **2023**, *3*, 100111. https://doi.org/10.1016/j.esci.2023.100111.
9. Zhao, M.; Chen, Z.; Shi, Y.; Hood, Z.D.; Lyu, Z.; Xie, M.; Chi, M.; Xia, Y. Kinetically Controlled Synthesis of Rhodium Nanocrystals with Different Shapes and a Comparison Study of Their Thermal and Catalytic Properties. *J. Am. Chem. Soc.* **2021**, *143*, 6293–6302. https://doi.org/10.1021/jacs.1c02734.
10. Zhou, S.; Liu, Y.; Li, J.; Liu, Z.; Shi, J.; Fan, L.; Cai, W. Surface-Neutralization Engineered NiCo-LDH/Phosphate Hetero-Sheets toward Robust Oxygen Evolution Reaction. *Green Energy Environ.* **2024**, *9*, 1151–1158. https://doi.org/10.1016/j.gee.2022.12.003.
11. Xie, J.; Zhang, Q.; Gu, L.; Xu, S.; Wang, P.; Liu, J.; Ding, Y.; Yao, Y.F.; Nan, C.; Zhao, M.; et al. Ruthenium–Platinum Core–Shell Nanocatalysts with Substantially Enhanced Activity and Durability towards Methanol Oxidation. *Nano Energy* **2016**, *21*, 247–257. https://doi.org/10.1016/j.nanoen.2016.01.013.

12. Wu, C.-Y.; Hsiao, Y.-C.; Chen, Y.; Lin, K.-H.; Lee, T.-J.; Chi, C.-C.; Lin, J.-T.; Hsu, L.-C.; Tsai, H.-J.; Gao, J.-Q.; et al. A Catalyst Family of High-Entropy Alloy Atomic Layers with Square Atomic Arrangements Comprising Iron- and Platinum-Group Metals. *Sci. Adv.* **2024**, *10*, eadl3693. https://doi.org/10.1126/sciadv.adl3693.
13. Qin, R.; Chen, G.; Feng, X.; Weng, J.; Han, Y. Ru/Ir-Based Electrocatalysts for Oxygen Evolution Reaction in Acidic Conditions: From Mechanisms, Optimizations to Challenges. *Adv. Sci.* **2024**, *11*, 2309364. https://doi.org/10.1002/advs.202309364.
14. Kumar, H.; Yan, M. Quantification of Nanomaterial Surfaces. *Mater. Interfaces* **2025**, *2*, 66–83. https://doi.org/10.53941/mi.2025.100007.
15. Hou, Y.; Cui, S.; Wen, Z.; Guo, X.; Feng, X.; Chen, J. Strongly Coupled 3D Hybrids of N-Doped Porous Carbon Nanosheet/CoNi Alloy-Encapsulated Carbon Nanotubes for Enhanced Electrocatalysis. *Small* **2015**, *11*, 5940–5948. https://doi.org/10.1002/smll.201502297.
16. Yan, Q.; Li, X.; Luo, J.; Zhao, M. Single-Molecule Fluorescence Imaging of Energy-Related Catalytic Reactions. *Chem. Biomed. Imaging* **2025**, *3*, 280–300. https://doi.org/10.1021/cbmi.4c00112.
17. Hammons, J.A.; Kang, S.; Ferron, T.J.; Aydin, F.; Lin, T.Y.; Seung, K.; Chow, P.; Xiao, Y.; Davis, J.T. Nanobubble Formation and Coverage during High Current Density Alkaline Water Electrolysis. *Nano Lett.* **2024**, *24*, 13695–13701. https://doi.org/10.1021/acs.nanolett.4c03657.
18. Wang, J.; Gao, Y.; Kong, H.; Kim, J.; Choi, S.; Ciucci, F.; Hao, Y.; Yang, S.; Shao, Z.; Lim, J. Non-Precious-Metal Catalysts for Alkaline Water Electrolysis: Operando Characterizations, Theoretical Calculations, and Recent Advances. *Chem. Soc. Rev* **2020**, *49*, 9154–9196. https://doi.org/10.1039/d0cs00575d.
19. Wang, J.; Xu, F.; Jin, H.; Chen, Y.; Wang, Y. Non-Noble Metal-Based Carbon Composites in Hydrogen Evolution Reaction: Fundamentals to Applications. *Adv. Mater.* **2017**, *29*, 1605838. https://doi.org/10.1002/adma.201605838.
20. Li, X.; Huang, C.; Han, W.; Ouyang, T.; Liu, Z. Transition Metal-Based Electrocatalysts for Overall Water Splitting. *Chin. Chem. Lett.* **2021**, *32*, 2597–2616. https://doi.org/10.1016/j.cclet.2021.01.047.
21. Pan, Q.; Wang, L. Recent Perspectives on the Structure and Oxygen Evolution Activity for Non-Noble Metal-Based Catalysts. *J. Power Sources* **2021**, *485*, 229335. https://doi.org/10.1016/j.jpowsour.2020.229335.
22. Gao, F.; Zhang, Y.; Wu, Z.; You, H.; Du, Y. Universal Strategies to Multi-Dimensional Noble-Metal-Based Catalysts for Electrocatalysis. *Coord. Chem. Rev.* **2021**, *436*, 213825. https://doi.org/10.1016/j.ccr.2021.213825.
23. Zubair, M.; Ul Hassan, M.; Mehran, M.; Baig, M.; Hussain, S.; Shahzad, F. 2D MXenes and Their Heterostructures for HER, OER and Overall Water Splitting: A Review. *Int. J. Hydrogen Energy* **2022**, *47*, 2794–2818. https://doi.org/10.1016/j.ijhydene.2021.10.248.
24. Wang, C.; Lin, Y.; Cui, L.; Zhu, J.; Bu, X. 2D Metal-Organic Frameworks as Competent Electrocatalysts for Water Splitting. *Small* **2023**, *19*, 2207342. https://doi.org/10.1002/smll.202207342.
25. Sun, S.; Jin, X.; Cong, B.; Zhou, X.; Hong, W.; Chen, G. Construction of Porous Nanoscale NiO/NiCo2O4 Heterostructure for Highly Enhanced Electrocatalytic Oxygen Evolution Activity. *J. Catal.* **2019**, *379*, 1–9. https://doi.org/10.1016/j.jcat.2019.09.010.
26. Cheng, H.; Wang, C.; Lyu, Z.; Zhu, Z.; Xia, Y. Controlling the Nucleation and Growth of Au on A-Se Nanospheres to Enhance Their Cellular Uptake and Cytotoxicity. *J. Am. Chem. Soc.* **2023**, *145*, 1216–1226. https://doi.org/10.1021/jacs.2c11053.
27. Cheng, H.; Zhou, S.; Xie, M.; Gilroy, K.D.; Zhu, Z.; Xia, Y. Colloidal Nanospheres of Amorphous Selenium: Facile Synthesis, Size Control, and Optical Properties. *Chem. Nano. Mater.* **2021**, *7*, 620–625. https://doi.org/10.1002/cnma.202100115.
28. Zheng, W.; Liu, M.; Lee, L.Y.S. Best Practices in Using Foam-Type Electrodes for Electrocatalytic Performance Benchmark. *ACS Energy Lett.* **2020**, *5*, 3260–3264. https://doi.org/10.1021/acsenergylett.0c01958.
29. Miyake, H.; Ye, S.; Osawa, M. Electroless Deposition of Gold Thin Films on Silicon for Surface-Enhanced Infrared Spectroelectrochemistry. *Electrochem. Commun.* **2002**, *4*, 973–977. https://doi.org/10.1016/S1388-2481(02)00510-6.
30. Ye, S.; Ichihara, T.; Uosaki, K. Spectroscopic Studies on Electroless Deposition of Copper on a Hydrogen-Terminated Si(111) Surface in Fluoride Solutions. *J. Electrochem. Soc.* **2001**, *148*, C421. https://doi.org/10.1149/1.1370964.
31. Mukherjee, S.; Mukhopadhyay, N.K.; Basu, J. Structural Modulation, Oriented Growth of Rock Salt, and Spinel in (Co(Cr/Mg)FeMnNi) Multicomponent Oxide and Derivatives. *J. Am. Ceram. Soc.* **2025**, *108*, e20619. https://doi.org/10.1111/jace.20619.
32. Park, J.; Kim, H.K.; Park, J.; Kim, B.; Baik, H.; Baik, M.-H.; Lee, K. Flattening Bent Janus Nanodiscs Expands Lattice Parameters. *Chem* **2023**, *9*, 948–962. https://doi.org/10.1016/j.chempr.2022.12.004.
33. Abidat, I.; Morais, C.; Comminges, C.; Canaff, C.; Rousseau, J.; Guignard, N.; Napporn, T.W.; Habrioux, A.; Kokoh, K.B. Three Dimensionally Ordered Mesoporous Hydroxylated NixCo3-xO4 Spinels for the Oxygen Evolution Reaction: On the Hydroxyl-Induced Surface Restructuring Effect. *J. Mater. Chem. A* **2017**, *5*, 7173–7183. https://doi.org/10.1039/c7ta00185a.

34. Anantharaj, S.; Noda, S. Appropriate Use of Electrochemical Impedance Spectroscopy in Water Splitting Electrocatalysis. *Chem. Electro. Chem.* **2020**, *7*, 2297–2308. https://doi.org/10.1002/celc.202000515.
35. Ruiz-Fresneda, M.A.; Eswayah, A.S.; Romero-González, M.; Gardiner, P.H.; Solari, P.L.; Merroun, M.L. Chemical and Structural Characterization of Se IV Biotransformations by Stenotrophomonas Bentonitica into Se^0 Nanostructures and Volatiles Se Species. *Environ. Sci. Nano* **2020**, *7*, 2140–2155. https://doi.org/10.1039/D0EN00507J.
36. Ariyoshi, K.; Siroma, Z.; Mineshige, A.; Takeno, M.; Fukutsuka, T.; Abe, T.; Uchida, S. Electrochemical Impedance Spectroscopy Part 1: Fundamentals. *Electrochemistry* **2022**, *90*, 102007. https://doi.org/10.5796/electrochemistry.22-66071.
37. Ding, J.; Du, M.; Wang, S.; Zhang, L.; Yue, Y.; Smedskjaer, M.M. Amorphous Material Based Heterostructures with Disordered Heterointerfaces for Advanced Rechargeable Batteries. *Energy Environ. Sci.* **2025**, *18*, 1587–1611. https://doi.org/10.1039/D4EE04566A.
38. Zou, X.; Liu, Y.; Li, G.; Wu, Y.; Liu, D.; Li, W.; Li, H.; Wang, D.; Zhang, Y.; Zou, X. Ultrafast Formation of Amorphous Bimetallic Hydroxide Films on 3D Conductive Sulfide Nanoarrays for Large-Current-Density Oxygen Evolution Electrocatalysis. *Adv. Mater.* **2017**, *29*, 1700404. https://doi.org/10.1002/adma.201700404.
39. Sun, J.; Xue, H.; Guo, N.; Song, T.; Hao, Y.; Sun, J.; Zhang, J.; Wang, Q. Synergetic Metal Defect and Surface Chemical Reconstruction into NiCo2S4/ZnS Heterojunction to Achieve Outstanding Oxygen Evolution Performance. *Angew. Chem. Int. Ed.* **2021**, *60*, 19435–19441. https://doi.org/10.1002/anie.202107731.
40. Jiang, J.; Sun, F.; Zhou, S.; Hu, W.; Zhang, H.; Dong, J.; Jiang, Z.; Zhao, J.; Li, J.; Yan, W.; et al. Atomic-Level Insight into Super-Efficient Electrocatalytic Oxygen Evolution on Iron and Vanadium Co-Doped Nickel (Oxy)Hydroxide. *Nat. Commun.* **2018**, *9*, 2885. https://doi.org/10.1038/s41467-018-05341-y.
41. Xue, Z.; Li, X.; Liu, Q.; Cai, M.; Liu, K.; Liu, M.; Ke, Z.; Liu, X.; Li, G. Interfacial Electronic Structure Modulation of NiTe Nanoarrays with NiS Nanodots Facilitates Electrocatalytic Oxygen Evolution. *Adv. Mater.* **2019**, *31*, 1900430. https://doi.org/10.1002/adma.201900430.
42. Niu, S.; Jiang, W.-J.; Wei, Z.; Tang, T.; Ma, J.; Hu, J.-S.; Wan, L.-J. Se-Doping Activates FeOOH for Cost-Effective and Efficient Electrochemical Water Oxidation. *J. Am. Chem. Soc.* **2019**, *141*, 7005–7013. https://doi.org/10.1021/jacs.9b01214.
43. Chen, J.; Qi, M.; Yang, Y.; Xiao, X.; Li, Y.; Jin, H.; Wang, Y. Chloride Residues in RuO2 Catalysts Enhance Its Stability and Efficiency for Acidic Oxygen Evolution Reaction. *Angew. Chem. Int. Ed.* **2025**, *64*, e202420860. https://doi.org/10.1002/anie.202420860.
44. Liu, X.; Zhao, P.; Liu, F.; Lin, R.; Yao, H.; Zhu, S. Attenuated Total Reflection Infrared Spectroscopy for Studying Electrochemical Cycling of Hydrogen, Carbon, and Nitrogen-Containing Molecules. *J. Energy Chem.* **2024**, *99*, 495–511. https://doi.org/10.1016/j.jechem.2024.08.008.